

The Speed of Sound in Methane under Conditions of the Thermal Boundary Layer of Uranus

Thomas G. White,^{1,2} Hannah Poole,² Emma E. McBride,^{3,4} Matthew Oliver,^{1,2,5} Adrien Descamps,^{3,4} Luke B. Fletcher,³ W. Alex Angermeier,¹ Cameron H. Allen,¹ Karen Appel,⁶ Florian P. Condamine,⁷ Chandra B. Curry,^{3,8} Francesco Dallari,⁹ Stefan Funk,¹⁰ Eric Galtier,³ Eliseo J. Gamboa,³ Maxence Gauthier,³ Peter Graham,¹¹ Sebastian Goede,⁶ Daniel Haden,¹ Jongjin B. Kim,³ Hae Ja Lee,³ Benjamin K. Ofori-Okai,³ Scott Richardson,¹¹ Alex Rigby,² Christopher Schoenwaelder,³ Peihao Sun,⁹ Bastian L. Witte,³ Thomas Tschentscher,⁶ Ulf Zastrau,⁶ Bob Nagler,³ Jerome Hastings,³ Giulio Monaco,⁹ Dirk O. Gericke,¹² Siegfried H. Glenzer,³ and Gianluca Gregori²

¹*Department of Physics, University of Nevada, Reno, Nevada 89557, USA*

²*Department of Physics, University of Oxford, Parks Road, Oxford OX1 3PU, UK*

³*SLAC National Accelerator Laboratory, 2575 Sand Hill Road, Menlo Park, California 94025, USA*

⁴*School of Mathematics and Physics, Queen's University Belfast, University Rd, Belfast BT7 1NN, UK*

⁵*Central Laser Facility, STFC Rutherford-Appleton Laboratory, Chilton, OX11 0QX, UK*

⁶*European XFEL GmbH, Holzkoppel 4, D-22869 Schenefeld, Germany*

⁷*Extreme Light Infrastructure ERIC, ELI Beamlines Facility,*

Za Radnici 835, 252 41 Dolni Brezany, Czech Republic

⁸*Department of Electrical and Computer Engineering, University of Alberta, Edmonton, Alberta T6G 1H9, Canada*

⁹*Dipartimento di Fisica e Astronomia "Galileo Galilei",*

Università degli Studi di Padova, Via F. Marzolo, 8, 35131 Padova, Italy

¹⁰*Erlangen Centre for Astroparticle Physics, Friedrich-Alexander-Universität Erlangen-Nürnberg,*

Erwin-Rommel-Str. 1, Erlangen D 91058, Germany

¹¹*AWE, Aldermaston, Reading, Berkshire RG7 4PR, United Kingdom*

¹²*Centre for Fusion, Space and Astrophysics, Department of Physics,*

University of Warwick, Coventry CV4 7AL, United Kingdom

(Dated: November 15, 2023)

We present the first direct observations of acoustic waves in warm dense matter. We analyze wavenumber- and energy-resolved X-ray spectra taken from warm dense methane created by laser-heating a cryogenic liquid jet. X-ray diffraction and inelastic free electron scattering yield sample conditions of 0.3 ± 0.1 eV and 0.8 ± 0.1 g/cm⁻³, corresponding to a pressure of ~ 13 GPa and matching the conditions predicted in the thermal boundary layer between the inner and outer envelope of Uranus. Inelastic X-ray scattering was used to observe the collective oscillations of the ions. With a highly improved energy resolution of ~ 50 meV, we could clearly distinguish the Brillouin peaks from the quasi-elastic Rayleigh feature. Data at different wavenumbers were used to obtain a sound speed of 5.9 ± 0.5 km/s, which enabled us to validate the use of Birch's law in this new parameter regime.

The state and evolution of methane-rich planets such as Uranus and Neptune are mainly determined by the properties of the dense, compressed matter in the planet interior [1–4]. One long-standing problem in planetary physics has been the inability of simple adiabatic models to explain the observed low luminosity of Uranus [5, 6]. However, recent non-adiabatic models have resolved this problem by including a thermal boundary layer (TBL) located at a radius of $\sim 20,000$ km - between the inner and outer envelopes - thus reducing internal cooling and lowering luminosity [7, 8]. Such models rely on accurate knowledge of thermodynamic and transport properties [9], with recent work prompting exploration of material properties in the 10–600 GPa and 1000–15,000 K range [8].

Compressed matter at these temperatures forms what is known as warm dense matter (WDM). WDM exhibits a complex interplay of factors, including partial ionization, electron quantum degeneracy, and strong ion-ion inter-

actions, making theoretical predictions challenging [10]. This complexity is particularly pronounced in carbon-bearing matter, where intriguing high-pressure chemistry unfolds [3, 11, 12]. While static material properties are well-constrained through a combination of experiments [3, 11, 13] and ab initio simulations [14–16], significant uncertainties persist in understanding dynamic and transport properties [17, 18]. One such vital property is the sound speed (c_s), which plays a crucial role in determining the adiabatic exponent [19], bulk modulus [20], and thermal conductivity [21, 22]. Quantifying these properties is essential for employing ring seismology techniques to explore the interiors of ice giants [19].

At elevated pressures, methane (CH₄) has been observed to conform to Birch's law [23, 24], where the sound speed shows a linear dependence on material density (ρ),

$$c_s \text{ [km/s]} = M\rho \text{ [g/cm}^3\text{]} + B. \quad (1)$$

This empirical relationship often serves as a basis for

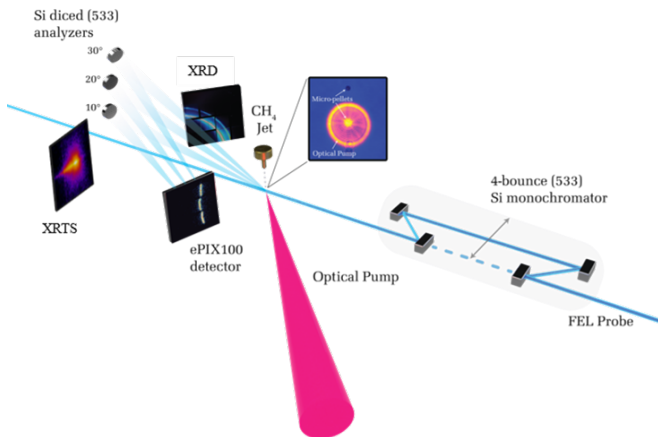


FIG. 1. Experimental setup showing the inelastic X-ray beam scattering off a fs-irradiated $5\ \mu\text{m}$ diameter cryogenic liquid methane jet at 5 Hz repetition rate. The energy of the scattered photons is determined using Si diced crystal analyzers at scattering angles of 10° ($Q=0.66\ \text{\AA}^{-1}$), 20° ($Q=1.32\ \text{\AA}^{-1}$), and 30° ($Q=1.96\ \text{\AA}^{-1}$). In the unmonochromized case, the angular spread of the photons (XRD) is captured on Cornell SLAC Pixel Array Detectors covering approximately $10^\circ - 50^\circ$ ($0.5 - 3.1\ \text{\AA}^{-1}$), while the inelastic component (XRTS) is measured using a HAPG crystal positioned at a scattering angle of 47° ($Q=3.03\ \text{\AA}^{-1}$).

extrapolating sound speeds to conditions within planetary interiors, with the coefficients $M = 13.2$ and $B = -4.7$ established through room temperature measurements [24]. However, the applicability of these coefficients at the higher temperatures found in planetary interiors remains untested. Indeed, in warm dense iron, the coefficients were found to vary considerably with temperature [20, 25, 26].

In this Letter, we describe the development and first application of high-resolution inelastic X-ray scattering to directly observe acoustic waves in methane at the conditions expected at the TBL. X-ray Thomson scattering (XRTS) utilizing high-intensity beams of penetrating radiation has emerged as a way to determine the microstructure and dynamics of extreme states of matter [27–31]. However, experiments have previously been limited to bandwidths of tens of eV for laser-produced X-rays [27] down to a few eV when using the seeded mode of X-ray free-electron lasers [30], whereas the energy shift caused by the collective ion motion is at a scale of just a few tens of meV. Combining improvements in free-electron laser technology with a silicon monochromator developed at synchrotron light sources, we were able to generate X-rays with sufficiently narrow bandwidths to distinguish the Brillouin peaks from the elastic Rayleigh peak. In our experiment, we achieved 50 meV energy resolution [32] and, for the first time, directly determined the sound speed in a WDM sample from the dispersion of the inelastic ion modes.

Figure 1 shows a schematic of the experiment performed at the Matter in Extreme Conditions (MEC) endstation at the Linac Coherent Light Source (LCLS). The incident X-ray pulse, with a central energy of 7492.1 eV and a 40 fs duration, was focused to a $\sim 5\ \mu\text{m}$ spot on the sample using a stack of beryllium compound refractive lenses. When measuring the collective motion of ions, a four-bounce silicon channel-cut (533) monochromator at a Bragg angle of 87.7° was driven into the beam to reduce the bandwidth to a nominal ~ 32 meV. To maximize the throughput of the monochromator, the seeded mode of LCLS was used. This mode has a bandwidth of ~ 1 eV (compared to ~ 20 eV in SASE mode), which significantly increased the fluence through the monochromator [33].

Three diced crystal analyzers [34] were positioned vertically at angles of 10° , 20° , and 30° , corresponding to scattering vectors Q of $0.66\ \text{\AA}^{-1}$, $1.32\ \text{\AA}^{-1}$, and $1.96\ \text{\AA}^{-1}$, respectively. The analyzers are made up of thousands of $1.5\ \text{mm} \times 1.5\ \text{mm}$ flat silicon crystals, which form a 10 cm-diameter spherically curved crystal. The spectrometer used energy-dispersive Johann geometry and was based on a Rowland circle with a diameter of 1 m and a Bragg angle matched to that of the monochromator. The spectrum measured by each individual flat crystal is combined on the detector, resulting in an increased signal. The overall energy resolution of the monochromator and diced crystal analyzer is ~ 50 meV over a range of ~ 500 meV. The scattered X-rays were collected on an ePIX100 detector with a $50\ \mu\text{m}$ pixel size [35]. We anticipate approximately 10^{10} photons per X-ray pulse reaching the sample, resulting in a beam intensity of $7.6 \times 10^{14}\ \text{W}/\text{cm}^2$. A detailed description of the spectrometer setup can be found in Ref. [32].

The sample consisted of cryogenic liquid methane droplets [36, 37] that were illuminated with the uncompressed short pulse Ti:Sapphire laser with an energy of 600 mJ at a wavelength of 800 nm. The spot was spatially and temporally Gaussian with a full-width half maximum of $100\ \mu\text{m}$ and 150 ps, respectively. The optical and X-ray laser pulses were overlapped 5 mm from the end of the jet nozzle to prevent potential damage. The replenishing jet target allowed the experiment to be run at a repetition rate of 5 Hz, allowing for considerably improved photon statistics compared to single-shot experiments.

Two ancillary diagnostics, XRTS with ~ 20 eV energy resolution and X-ray diffraction (XRD), characterized the thermodynamic state of the system. Both diagnostics were run without the monochromator in place to maximize signal levels. The XRD employed a Cornell Stanford Pixelated Area Detector (CSPAD) placed approximately 100 mm from the interaction point covering a 2θ range of $10 - 50$ degrees ($0.5 - 3.1\ \text{\AA}^{-1}$). Processing and integration of the powder patterns were carried out using the Dioptas software [39], and the diagnostic was calibrated using X-ray diffraction from polycrystalline LaB6 [38].

Figure 2 shows the evolution of the angular-resolved

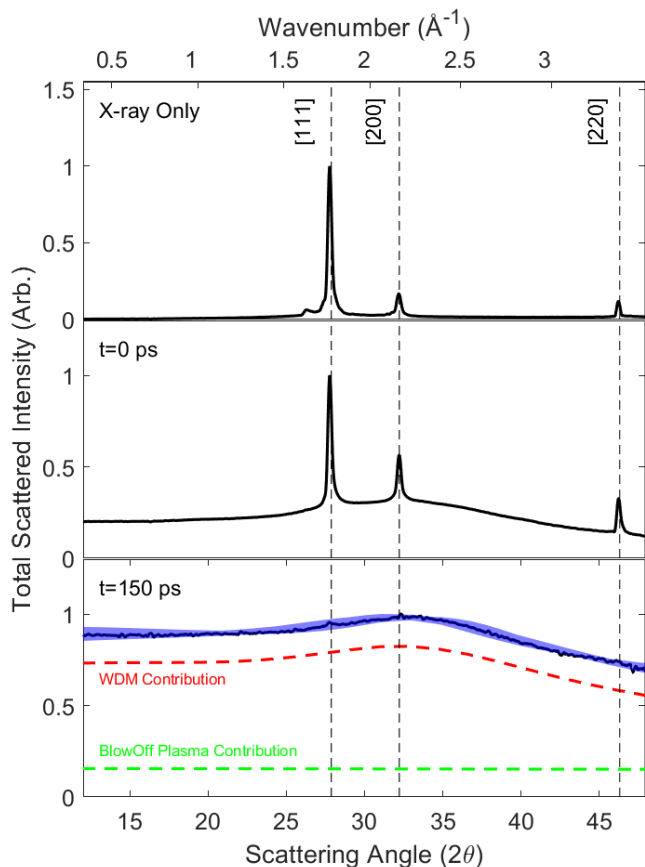


FIG. 2. Angular-resolved X-ray diffraction (XRD) data. (Top) Bragg peaks from Debye-Scherrer rings indicative of an fcc lattice of methane at a density of 0.5 g/cm^3 are observed. (Middle) During the laser pulse, we observe the emergence of a broad liquid diffraction peak concurrently with Bragg peaks of reduced intensity. (Bottom) The Bragg peaks are significantly weakened and the signal is dominated by liquid diffraction. The shaded region shows the range of accepted fits corresponding to thermodynamic conditions given in Tab. I. The red and green curves show the relative contribution from the WDM and blow-off plasma states.

scattering as a function of laser delay. When no optical laser is present (‘X-ray Only’), we see three distinct Bragg peaks. These are consistent with methane forming face-centered-cubic (fcc) crystallites as it freezes when exiting the nozzle. From the Bragg peak positions, we infer a density of 0.5 g/cm^3 . At 0 ps, which corresponds to the X-ray pulse arriving at the peak of the drive laser, we see the coexistence of the solid and liquid phases, with the intensity of the Bragg peaks decreasing and a broad ion-liquid correlation peak emerging. At an additional delay of 150 ps, the signal is dominated by a broad liquid correlation peak.

The XRTS spectrum was collected on a cylindrically curved, highly annealed pyrolytic graphite (HAPG) crystal in von Hamos geometry. The spectrometer was positioned at an average scattering angle of 47° , with an

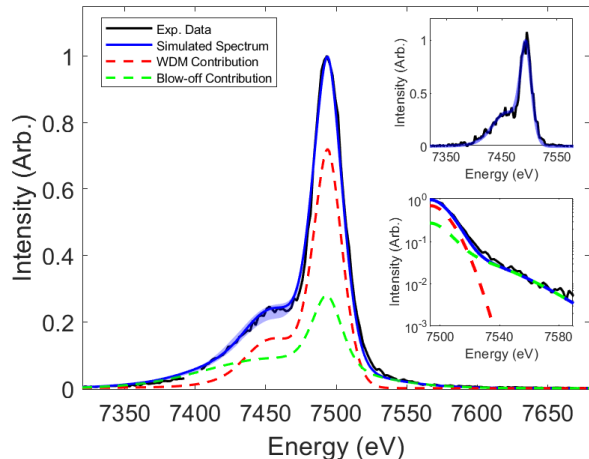


FIG. 3. X-ray Thomson Scattering Spectra at 47° for methane at 150 ps delay. The experimental data (black line) are fitted with theoretical dynamic structure factor calculations. The experimental data are well fitted with scattering from two regions with distinct thermodynamic conditions, one coming from the dense methane plasma (red) and a second from a hot low-density blow-off plasma (green). The blue-shaded region highlights the range of spectra accepted in the MCMC fitting procedure described in the main text. The top inset shows the spectrum corresponding to undriven methane. The bottom inset highlights the high-energy wing of the Compton feature, which is used to constrain the temperature of the blow-off plasma [38, 46].

acceptance angle of 7° . The spectrum was captured on an ePix100 detector with a $50 \mu\text{m}$ pixel size. The energy dispersion was found to be 1.93 eV/px , calibrated using fluorescence of the $K_{\beta 1}$ line of iron [40]. Fig. 3 shows the spectrum collected at a time delay of 150 ps, coinciding with the XRD signal shown in the bottom panel of Fig. 2. In addition to a reduction in inelastic scattering due to the heating and compression of the methane, the modified spectrum now contains a significant scattering contribution from a hot blow-off plasma surrounding the irradiated target, as highlighted by the large free-free Compton feature visible in the bottom inset. The top inset of Fig. 3 shows the scattered spectrum for undriven methane, which is consistent with a synthetic spectrum [41–45] calculated for a density of 0.5 g/cm^3 at $\sim 0 \text{ eV}$, confirming the density inferred from the XRD data.

A method for exploring the complex multi-parameter space is to utilize Bayesian inference using Markov-Chain Monte Carlo (MCMC) [47, 48]. Given a specific set of parameters, $\Theta(T_e, \rho, Z_H, Z_C, r_c)$, the MCMC process calculates the likelihood of these sets producing the given experimental spectrum and provides a robust estimate of the errors. Two separate MCMC explorations were run for the XRTS and XRD data. Each assumed two uniform plasma conditions, one representing the WDM conditions and the other the blow-off conditions. The

blow-off plasma was found to be at $T_e = 36$ eV and assumed to be at a low density, $\rho < 0.05$ g/cm³. At these conditions, the ionization of the two species is estimated to be $Z_C = 4$, $Z_H = 1$ [49]. The regions were weighted by the parameter r_c , equal to the fraction of scattering from WDM determined to contribute to the overall signal. Additional details on the MCMC procedure are provided in the supplementary material [38].

The range of accepted spectra are shown as blue shaded regions in figures 2 and 3 for the XRD and XRTS diagnostics, respectively. Tab. I shows the inferred thermodynamic properties of the compressed, warm methane after combining the XRTS and XRD MCMC information. The error on each parameter is quoted as the 1σ deviation from the mean. The values of density and temperature with the highest likelihood are 0.3 eV (3480 K) and 0.8 g cm⁻³, corresponding to a pressure of ~ 13 GPa found from ab-initio density functional theory [8, 14]. The thermodynamic conditions achieved in the experiment match the conditions predicted at the TBL of Uranus [6–8], also shown in Tab. I.

The high-resolution inelastic X-ray scattering spectra are shown in Fig. 4. The three detectors are situated in the collective scattering regime [42], exhibiting scattering parameters ($\alpha = 1/Q\lambda_s$) of 13.8, 6.9, and 4.6. These values were computed using a Debye screening length of $\lambda_s = 0.11$ Å, utilizing the thermodynamic parameters in Table I. Using scattering from undriven methane, shown by the blue lines in Fig. 4, the instrument function for the analyzers was found to have a full-width half-maximum (FWHM) of 49 meV, 42 meV, and 46 meV for 10°, 20°, and 30°, respectively. These values were found to be consistent with the calculated value of 46 meV [32].

The driven case is shown by the red lines in Fig. 4. On the 30° detector, which corresponds to the highest scattering vector, Brillouin peaks were observed at an energy transfer of around 75 meV on either side of the Rayleigh peak. Furthermore, as a consequence of detailed balance, the height of the downshifted peak is larger than the upshifted peak. In this case, the intensity ratio between the two peaks is 0.8 ± 0.1 , corresponding to an ion temperature of roughly 0.3 eV - in agreement with the electron

TABLE I. Comparison of the experimental thermodynamic conditions of the methane plasma with conditions predicted at the TBL of Uranus. The experimental error bars are obtained from the MCMC fitting procedure [38].

Parameter	Experiment	TBL [6–8]
T_e (eV)	0.3 ± 0.1	0.2 - 0.6
ρ (g/cm ³)	0.8 ± 0.1	0.3 - 1.5
P (GPa)	13 ± 1 [8, 14]	10 - 15
Z_C	0.4 ± 0.1	
Z_H	0.4 ± 0.1	
r_c	0.73 ± 0.01	

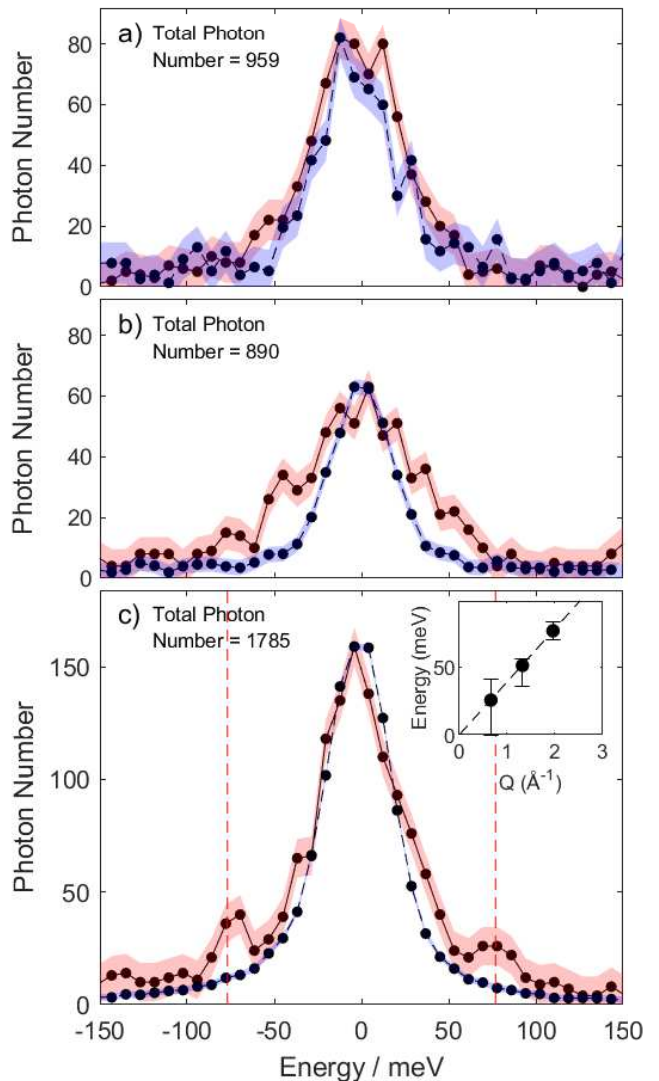


FIG. 4. High-resolution inelastic X-ray scattering spectrum taken at (a) 10°, (b) 20°, and (c) 30° for driven (red) and undriven (blue) methane. The shaded areas indicate the Poisson noise limit, which is equal to \sqrt{N}/N . The data consists of 5965 events and the number of photons collected in each case is shown. The data is presented in bins with a width of 8.2 meV, corresponding to a single pixel on the detector. The vertical dashed lines show the predicted peak position for an acoustic wave with a sound speed of 5.9 km/s. The inset shows the dispersion relation obtained by fitting each spectrum with a combination of three Voigt profiles [38], with the dashed line corresponding to the measured acoustic wave speed.

temperature measured through XRTS and XRD. On the detector positioned at the 20° scattering angle, the Brillouin peaks are not well resolved, instead appearing as additional shoulders on either side of the Rayleigh peak. Finally, no additional broadening was observed on the detector positioned at 10°.

In the visco-elastic regime, the shape of the scattering spectrum can be described in terms of Q and ω dependent transport coefficients [50, 51]. In our case, the low photon number and consequential energy resolution preclude accurate extraction of such quantities directly from the shape and width of the spectrum. Nevertheless, a more robust measurement is the determination of the acoustic wave speed from the Brillouin peak positions. In the hydrodynamic regime ($\alpha < 2.32$ or, equivalently, $Q < 0.43/\lambda_s = 3.9 \text{ \AA}^{-1}$), these positions exhibit a linear shift with Q [52], consistent with the data. In our case, the peak position on the 30° detector matches an acoustic wave speed of $5.9 \pm 0.5 \text{ km/s}$, as shown by the red vertical dashed lines in Fig. 4. The inset of 4c shows the dispersion relation obtained by fitting each of the driven spectra with a combination of three Voigt profiles [38], with the dashed line corresponding to an acoustic wave speed of $5.9 \pm 0.5 \text{ km/s}$.

Our realization of high-resolution X-ray scattering has enabled us to investigate the acoustic waves and measure the sound speed for the extreme conditions expected at the TBL in non-adiabatic models of Uranus. Our sound speed measurement is consistent with Eq. 1, which for a density of 0.8 g/cm^3 predicts a sound speed of 5.86 km/s , validating the use of Birch's law at temperatures as high as 0.3 eV (3480 K). This measurement represents a reliable benchmark for equation-of-state models applied in this region, surpassing the limitations imposed by solely static thermodynamic properties or the microscopic structure. Moreover, the ion dynamics holds further information on the particle interactions. Testing the accuracy of EOS models holds immense importance for advancing comprehensive descriptions of the formation, thermal evolution, and internal structure of the ice giants within our solar system and intermediate-size exoplanets. The sound speeds in this regime also play a pivotal role in the field of giant planet seismology, enabling us to employ Uranus quakes and ring seismology as tools to unravel the planet's internal composition [19, 53, 54].

In summary, we have demonstrated a novel X-ray scattering platform capable of assessing elemental properties, here sound speeds, within high-pressure and high-temperature states akin to those found in planets of our solar system and exoplanets. Notably, we have successfully determined the sound speed of methane under pressure-temperature conditions matching those anticipated at the Uranus TBL, and have confirmed its consistency with Birch's law.

TGW thanks Yafis Barlas for valuable discussions. This material is partially based upon work supported by the U.S. Department of Energy, Office of Science, Office of Fusion Energy Sciences (Award No. DE-SC0019268) and the National Nuclear Security Administration (NNSA) (Award No. DE-NA0004039). This work was supported by the UK Research & Innovation Future Leaders Fellowship (MR/W008211/1) and by the

Science and Technologies Facilities Council under grant no. ST/W000903/1. K.A. and T.T. acknowledge support from the DFG (Grant No. FOR 2440). The work of C.B.C. was supported by the U.S. DOE Office of Science, Fusion Energy Sciences under FWP No. 100182. C.B.C. acknowledges partial support from the Natural Sciences and Engineering Research Council of Canada (NSERC). Use of the Linac Coherent Light Source, SLAC National Accelerator Laboratory, is supported by the U.S. Department of Energy, Office of Science, Office of Basic Energy Sciences under Contract No. DE-AC02-76SF00515. The MEC instrument is supported by the U.S. Department of Energy, Office of Science, Office of Fusion Energy Sciences under Contract No. DE-AC02-76SF00515.

-
- [1] T. Guillot, Interiors of Giant Planets Inside and Outside the Solar System, *Science* **286**, 72 (1999).
 - [2] M. D. Knudson, M. P. Desjarlais, R. W. Lemke, T. R. Mattsson, M. French, N. Nettelmann, and R. Redmer, Probing the Interiors of the Ice Giants: Shock Compression of Water to 700 GPa and 3.8 g/cm^3 , *Phys. Rev. Lett.* **108**, 091102 (2012).
 - [3] D. Kraus, J. Vorberger, A. Pak, N. J. Hartley, L. B. Fletcher, S. Frydrych, E. Galtier, E. J. Gamboa, D. O. Gericke, S. H. Glenzer, E. Granados, M. J. MacDonald, A. J. MacKinnon, E. E. McBride, I. Nam, P. Neumayer, M. Roth, A. M. Saunders, A. K. Schuster, P. Sun, T. van Driel, T. Döppner, and R. W. Falcone, Formation of diamonds in laser-compressed hydrocarbons at planetary interior conditions, *Nature Astronomy* **1**, 606 (2017).
 - [4] M. Ross, The ice layer in Uranus and Neptune—diamonds in the sky?, *Nature* **292**, 435 (1981).
 - [5] N. Nettelmann, R. Helled, J. Fortney, and R. Redmer, New indication for a dichotomy in the interior structure of Uranus and Neptune from the application of modified shape and rotation data, *Planetary and Space Science* **77**, 143 (2013).
 - [6] R. Helled, N. Nettelmann, and T. Guillot, Uranus and Neptune: Origin, Evolution and Internal Structure, *Space Science Reviews* **216**, 38 (2020).
 - [7] Vazan, Allona and Helled, Ravit, Explaining the low luminosity of Uranus: A self-consistent thermal and structural evolution, *A&A* **633**, A50 (2020).
 - [8] N. Nettelmann, K. Wang, J. Fortney, S. Hamel, S. Yellamilli, M. Bethkenhagen, and R. Redmer, Uranus evolution models with simple thermal boundary layers, *Icarus* **275**, 107 (2016).
 - [9] U. R. Christensen, V. Holzwarth, and A. Reiners, Energy flux determines magnetic field strength of planets and stars, *Nature* **457**, 167 (2009).
 - [10] S. Ichimaru, *Statistical Plasma Physics, Volume II: Condensed Plasmas*, Frontiers in Physics (CRC Press, 2018).
 - [11] L. R. Benedetti, J. H. Nguyen, W. A. Caldwell, H. Liu, M. Kruger, and Raymond Jeanloz, Dissociation of CH₄ at high pressures and temperatures: Diamond formation in giant planet interiors?, *Science* **286**, 100 (1999).
 - [12] D. Kraus, N. J. Hartley, S. Frydrych, A. K. Schuster, K. Rohatsch, M. Rödel, T. E. Cowan, S. Brown, E. Cun-

- ningham, T. van Driel, L. B. Fletcher, E. Galtier, E. J. Gamboa, A. Laso Garcia, D. O. Gericke, E. Granados, P. A. Heimann, H. J. Lee, M. J. MacDonald, A. J. MacKinnon, E. E. McBride, I. Nam, P. Neumayer, A. Pak, A. Pelka, I. Prencipe, A. Ravasio, R. Redmer, A. M. Saunders, M. Schölmerich, M. Schörner, P. Sun, S. J. Turner, A. Zettl, R. W. Falcone, S. H. Glenzer, T. Döppner, and J. Vorberger, High-pressure chemistry of hydrocarbons relevant to planetary interiors and inertial confinement fusion, *Physics of Plasmas* **25**, 056313 (2018).
- [13] W. J. Nellis, D. C. Hamilton, and A. C. Mitchell, Electrical conductivities of methane, benzene, and polybutene shock compressed to 60 GPa (600 kbar), *The Journal of Chemical Physics* **115**, 1015 (2001).
- [14] B. L. Sherman, H. F. Wilson, D. Weeraratne, and B. Militzer, Ab initio simulations of hot dense methane during shock experiments, *Phys. Rev. B* **86**, 224113 (2012).
- [15] F. Ancilotto, G. L. Chiarotti, S. Scandolo, and E. Tosatti, Dissociation of methane into hydrocarbons at extreme (planetary) pressure and temperature, *Science* **275**, 1288 (1997).
- [16] N. Goldman, E. J. Reed, and L. E. Fried, Quantum mechanical corrections to simulated shock Hugoniot temperatures, *The Journal of Chemical Physics* **131**, 204103 (2009).
- [17] P. Grabowski, S. Hansen, M. Murillo, L. Stanton, F. Graziani, A. Zylstra, S. Baalrud, P. Arnault, A. Baczewski, L. Benedict, C. Blancard, O. Čertík, J. Clérouin, L. Collins, S. Copeland, A. Correa, J. Dai, J. Daligault, M. Desjarlais, M. Dharma-wardana, G. Faussurier, J. Haack, T. Haxhimali, A. Hayes-Sterbenz, Y. Hou, S. Hu, D. Jensen, G. Jungman, G. Kagan, D. Kang, J. Kress, Q. Ma, M. Marciantie, E. Meyer, R. Rudd, D. Saumon, L. Shulenburger, R. Singleton, T. Sjostrom, L. Stanek, C. Starrett, C. Ticknor, S. Valaitis, J. Venzke, and A. White, Review of the first charged-particle transport coefficient comparison workshop, *High Energy Density Physics* **37**, 100905 (2020).
- [18] T. G. White, J. Dai, and D. Riley, Dynamic and transient processes in warm dense matter, *Philosophical Transactions of the Royal Society A: Mathematical, Physical and Engineering Sciences* **381**, 20220223 (2023).
- [19] J. A. A'Hearn, M. M. Hedman, C. R. Mankovich, H. Aramona, and M. S. Marley, Ring seismology of the ice giants uranus and neptune, *The Planetary Science Journal* **3**, 194 (2022).
- [20] D. Ikuta, E. Ohtani, H. Fukui, T. Sakai, D. Ishikawa, and A. Q. R. Baron, Sound velocity of hexagonal close-packed iron to the Earth's inner core pressure, *Nature Communications* **13**, 7211 (2022).
- [21] P. W. Bridgman, The Thermal Conductivity of Liquids under Pressure, *Proceedings of the American Academy of Arts and Sciences* **59**, 141 (1923).
- [22] S. A. Khrapak, Bridgman formula for the thermal conductivity of atomic and molecular liquids, *Journal of Molecular Liquids* **381**, 121786 (2023).
- [23] F. Birch, Density and composition of mantle and core, *Journal of Geophysical Research (1896-1977)* **69**, 4377 (1964).
- [24] D. W. Meyer, W.-P. Hsieh, H. Hsu, C.-Y. Kuo, and J.-F. Lin, Thermal Conductivity and Compressional Velocity of Methane at High Pressure: Insights Into Thermal Transport Properties of Icy Planet Interiors, *Journal of Geophysical Research: Planets* **127**, e2021JE007059 (2022).
- [25] T. Sakamaki, E. Ohtani, H. Fukui, S. Kamada, S. Takahashi, T. Sakairi, A. Takahata, T. Sakai, S. Tsutsui, D. Ishikawa, R. Shiraishi, Y. Seto, T. Tsuchiya, and A. Q. R. Baron, Constraints on Earth's inner core composition inferred from measurements of the sound velocity of hcp-iron in extreme conditions, *Science Advances* **2**, e1500802 (2016).
- [26] J. Bouchet, F. Bottin, D. Antonangeli, and G. Morard, Sound velocities and thermodynamical properties of hcp iron at high pressure and temperature, *Journal of Physics: Condensed Matter* **34**, 344002 (2022).
- [27] S. H. Glenzer, G. Gregori, R. W. Lee, F. J. Rogers, S. W. Pollaine, and O. L. Landen, Demonstration of spectrally resolved X-ray scattering in dense plasmas, *Phys. Rev. Lett.* **90**, 175002 (2003).
- [28] S. H. Glenzer, O. L. Landen, P. Neumayer, R. W. Lee, K. Widmann, S. W. Pollaine, R. J. Wallace, G. Gregori, A. Höll, T. Bornath, R. Thiele, V. Schwarz, W.-D. Kraeft, and R. Redmer, Observations of plasmons in warm dense matter, *Phys. Rev. Lett.* **98**, 065002 (2007).
- [29] T. Ma, T. Döppner, R. W. Falcone, L. Fletcher, C. Fortmann, D. O. Gericke, O. L. Landen, H. J. Lee, A. Pak, J. Vorberger, K. Wünsch, and S. H. Glenzer, X-ray scattering measurements of strong ion-ion correlations in shock-compressed aluminum, *Phys. Rev. Lett.* **110**, 065001 (2013).
- [30] L. B. Fletcher, H. J. Lee, T. Döppner, E. Galtier, B. Nagler, P. Heimann, C. Fortmann, S. LePape, T. Ma, M. Millot, A. Pak, D. Turnbull, D. A. Chapman, D. O. Gericke, J. Vorberger, T. White, G. Gregori, M. Wei, B. Barbrel, R. W. Falcone, C.-C. Kao, H. Nuhn, J. Welch, U. Zastrau, P. Neumayer, J. B. Hastings, and S. H. Glenzer, Ultrabright X-ray laser scattering for dynamic warm dense matter physics, *Nature Photonics* **9**, 274 (2015).
- [31] T. Döppner, M. Bethkenhagen, D. Kraus, P. Neumayer, D. A. Chapman, B. Bachmann, R. A. Baggott, M. P. Böhme, L. Divol, R. W. Falcone, L. B. Fletcher, O. L. Landen, M. J. MacDonald, A. M. Saunders, M. Schörner, P. A. Sterne, J. Vorberger, B. B. L. Witte, A. Yi, R. Redmer, S. H. Glenzer, and D. O. Gericke, Observing the onset of pressure-driven K-shell delocalization, *Nature* **618**, 270 (2023).
- [32] E. E. McBride, T. G. White, A. Descamps, L. B. Fletcher, K. Appel, F. P. Condamine, C. B. Curry, F. Dallari, S. Funk, E. Galtier, M. Gauthier, S. Goede, J. B. Kim, H. J. Lee, B. K. Ofori-Okai, M. Oliver, A. Rigby, C. Schoenwaelder, P. Sun, Th. Tschentscher, B. B. L. Witte, U. Zastrau, G. Gregori, B. Nagler, J. Hastings, S. H. Glenzer, and G. Monaco, Setup for meV-resolution inelastic X-ray scattering measurements and X-ray diffraction at the Matter in Extreme Conditions endstation at the Linac Coherent Light Source, *Review of Scientific Instruments* **89**, 10F104 (2018).
- [33] A. Descamps, B. K. Ofori-Okai, J. K. Baldwin, Z. Chen, L. B. Fletcher, S. H. Glenzer, N. J. Hartley, J. B. Hasting, D. Khaghani, M. Mo, B. Nagler, V. Recoules, R. Redmer, M. Schörner, P. Sun, Y. Q. Wang, T. G. White, and E. E. McBride, Towards performing high-resolution inelastic X-ray scattering measurements at hard X-ray free-electron lasers coupled with energetic laser drivers, *Journal of Synchrotron Radiation* **29**, 931 (2022).
- [34] R. Verbeni, M. Kocsis, S. Huotari, M. Krisch, G. Monaco,

- F. Sette, and G. Vanko, Advances in crystal analyzers for inelastic X-ray scattering, *Journal of Physics and Chemistry of Solids* **66**, 2299 (2005).
- [35] G. Blaj, P. Caragiulo, G. Carini, S. Carron, A. Dragone, D. Freytag, G. Haller, P. Hart, J. Hasi, R. Herbst, S. Herrmann, C. Kenney, B. Markovic, K. Nishimura, S. Osier, J. Pines, B. Reese, J. Segal, A. Tomada, and M. Weaver, X-ray detectors at the linac coherent light source, *Journal of Synchrotron Radiation* **22**, 577 (2015).
- [36] J. B. Kim, C. Schoenwaelder, and S. H. Glenzer, Development and characterization of liquid argon and methane microjets for high-rep-rate laser-plasma experiments, *Review of Scientific Instruments* **89**, 10K105 (2018).
- [37] C. B. Curry, C. Schoenwaelder, S. Goede, J. B. Kim, M. Rehwald, F. Treffert, K. Zeil, S. H. Glenzer, M. Gauthier, C. B. Curry, J. B. Kim, and S. H. Glenzer, Cryogenic Liquid Jets for High Repetition Rate Discovery Science, *JoVE*, e61130 (2020).
- [38] See Supplemental Material at [URL will be inserted by publisher] for details of the MCMC fitting procedure, detector calibration, additional spectra for undriven samples, and Voigt fitting of driven spectra.
- [39] C. Prescher and V. B. Prakapenka, DIOPTAS: A program for reduction of two-dimensional X-ray diffraction data and data exploration, *High Pressure Research* **35**, 223 (2015).
- [40] J. A. Bearden, X-ray wavelengths, *Rev. Mod. Phys.* **39**, 78 (1967).
- [41] D. Pines and D. Bohm, A collective description of electron interactions: II. Collective vs individual particle aspects of the interactions, *Phys. Rev.* **85**, 338 (1952).
- [42] S. H. Glenzer and R. Redmer, X-ray Thomson scattering in high energy density plasmas, *Rev. Mod. Phys.* **81**, 1625 (2009).
- [43] G. Gregori, S. H. Glenzer, F. J. Rogers, S. M. Pollaine, O. L. Landen, C. Blancard, G. Faussurier, P. Renaudin, S. Kuhlbrodt, and R. Redmer, Electronic structure measurements of dense plasmas, *Physics of Plasmas* **11**, 2754 (2004).
- [44] G. Gregori, A. Ravasio, A. Höll, S. Glenzer, and S. Rose, Derivation of the static structure factor in strongly coupled non-equilibrium plasmas for X-ray scattering studies, *High Energy Density Physics* **3**, 99 (2007).
- [45] G. Gregori, S. H. Glenzer, W. Rozmus, R. W. Lee, and O. L. Landen, Theoretical model of x-ray scattering as a dense matter probe, *Phys. Rev. E* **67**, 026412 (2003).
- [46] T. Döppner, A. L. Kritcher, D. Kraus, S. H. Glenzer, B. L. Bachmann, D. Chapman, G. W. Collins, R. W. Falcone, J. Hawreliak, O. L. Landen, H. J. Lee, S. L. Pape, T. Ma, P. Neumayer, R. Redmer, and D. C. Swift, X-ray Thomson scattering as a temperature probe for Gbar shock experiments, *Journal of Physics: Conference Series* **500**, 192019 (2014).
- [47] M. F. Kasim, T. P. Galligan, J. Topp-Mugglestone, G. Gregori, and S. M. Vinko, Inverse problem instabilities in large-scale modeling of matter in extreme conditions, *Physics of Plasmas* **26**, 112706 (2019).
- [48] H. Poole, D. Cao, R. Epstein, I. Golovkin, T. Walton, S. X. Hu, M. Kasim, S. M. Vinko, J. R. Rygg, V. N. Goncharov, G. Gregori, and S. P. Regan, A case study of using x-ray Thomson scattering to diagnose the in-flight plasma conditions of DT cryogenic implosions, *Physics of Plasmas* **29**, 072703 (2022).
- [49] J. MacFarlane, I. Golovkin, and P. Woodruff, HELIOS-CR – A 1-D radiation-magnetohydrodynamics code with inline atomic kinetics modeling, *Journal of Quantitative Spectroscopy and Radiative Transfer* **99**, 381 (2006).
- [50] J. Boon and S. Yip, *Molecular Hydrodynamics*, Dover Books on Physics (Dover Publications, 1991).
- [51] R. Schmidt, B. J. B. Crowley, J. Mithen, and G. Gregori, Quantum hydrodynamics of strongly coupled electron fluids, *Phys. Rev. E* **85**, 046408 (2012).
- [52] J. P. Mithen, J. Daligault, and G. Gregori, Extent of validity of the hydrodynamic description of ions in dense plasmas, *Phys. Rev. E* **83**, 015401(R) (2011).
- [53] T. Guillot, Uranus and Neptune are key to understand planets with hydrogen atmospheres, *Experimental Astronomy* **54**, 1027 (2022).
- [54] S. Markham and D. Stevenson, Excitation mechanisms for Jovian seismic modes, *Icarus* **306**, 200 (2018).

Supplementary Material for “The Speed of Sound in Methane under Conditions of the Thermal Boundary Layer of Uranus”

Thomas G. White,^{1,2} Hannah Poole,² Emma E. McBride,^{3,4} Matthew Oliver,^{1,2,5} Adrien Descamps,^{3,4} Luke B. Fletcher,³ W. Alex Angermeier,¹ Cameron H. Allen,¹ Karen Appel,⁶ Florian P. Condamine,⁷ Chandra B. Curry,^{3,8} Francesco Dallari,⁹ Stefan Funk,¹⁰ Eric Galtier,³ Eliseo J. Gamboa,³ Maxence Gauthier,³ Peter Graham,¹¹ Sebastian Goede,⁶ Daniel Haden,¹ Jongjin B. Kim,³ Hae Ja Lee,³ Benjamin K. Ofori-Okai,³ Scott Richardson,¹¹ Alex Rigby,² Christopher Schoenwaelder,³ Peihao Sun,⁹ Bastian L. Witte,³ Thomas Tschentscher,⁶ Ulf Zastrau,⁶ Bob Nagler,³ Jerome Hastings,³ Giulio Monaco,⁹ Dirk O. Gericke,¹² Siegfried H. Glenzer,³ and Gianluca Gregori²

¹*Department of Physics, University of Nevada, Reno, Nevada 89557, USA*

²*Department of Physics, University of Oxford, Parks Road, Oxford OX1 3PU, UK*

³*SLAC National Accelerator Laboratory, 2575 Sand Hill Road, Menlo Park, California 94025, USA*

⁴*School of Mathematics and Physics, Queen’s University Belfast, University Rd, Belfast BT7 1NN, UK*

⁵*Central Laser Facility, STFC Rutherford-Appleton Laboratory, Chilton, OX11 0QX, UK*

⁶*European XFEL GmbH, Holzkoppel 4, D-22869 Schenefeld, Germany*

⁷*Extreme Light Infrastructure ERIC, ELI Beamlines Facility,*

Za Radnici 835, 252 41 Dolni Brezany, Czech Republic

⁸*Department of Electrical and Computer Engineering,*

University of Alberta, Edmonton, Alberta T6G 1H9, Canada

⁹*Dipartimento di Fisica e Astronomia “Galileo Galilei”,*

Università degli Studi di Padova, Via F. Marzolo, 8, 35131 Padova, Italy

¹⁰*Erlangen Centre for Astroparticle Physics, Friedrich-Alexander-Universität Erlangen-Nürnberg,*

Erwin-Rommel-Str. 1, Erlangen D 91058, Germany

¹¹*AWE, Aldermaston, Reading, Berkshire RG7 4PR, United Kingdom*

¹²*Centre for Fusion, Space and Astrophysics, Department of Physics,*

University of Warwick, Coventry CV4 7AL, United Kingdom

(Dated: November 15, 2023)

DETAILS OF THE XRTS AND XRD CODE

The analysis of the XRTS and XRD data was performed using an X-ray scattering model [1]. The source function was assumed as an exponentially modified Gaussian distribution,

$$f(E) = \frac{1}{2^{\frac{\gamma+1}{\gamma}} a \Gamma\left(\frac{\gamma+1}{\gamma}\right)} \exp\left[-\frac{|(E - \mu)/a|^\gamma}{2}\right] \quad (1)$$

where Γ is the Gamma function, $\mu = 7.492$ keV, $a = \text{FWHM}/2$ with $\text{FWHM} = 20$ eV and $\gamma = 1.8$. The source parameters were determined by fitting the scattering signal from the driven methane (shown in Fig. 3 of the main manuscript and reproduced in Fig. 1 without the additional Bayesian analysis. The scattering model calculates the X-ray dynamic structure factor for a given set of parameters. This structure factor contains the contributions that arise from the scattering from free, weakly bound (including bound-free transitions), and tightly bound electrons. The first term is typically defined using the random phase approximation (RPA) [2], appropriate for ideal collisionless plasmas. Whilst this can be used to model the blow-off plasma, for the WDM core, dynamic local field corrections (LFC) [3] have been used. The bound-free feature is treated using the impulse approximation (IA) [4], which assumes that the electron-photon interaction occurs on a very short time scale. The last term is determined using the static screened one-component plasma (SOCP) model [5].

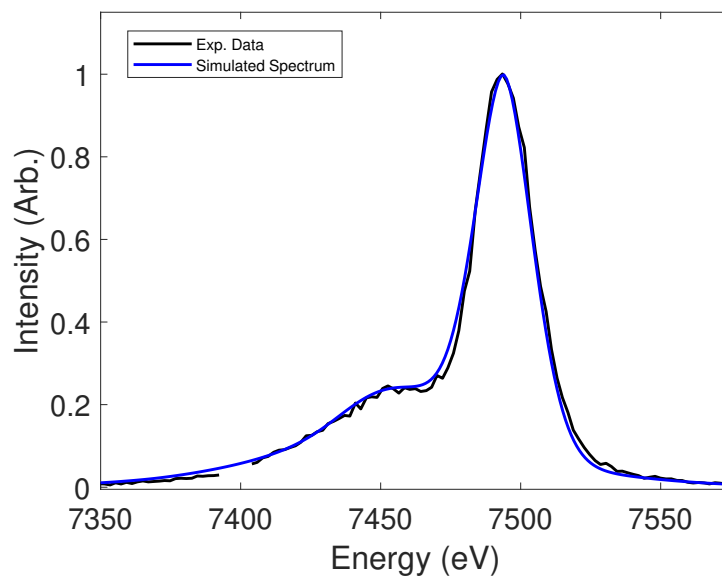


FIG. 1. X-ray Thomson Scattering Spectra at 47° for methane at 150 ps delay, reproduced from Fig. 3 in the main manuscript without the additional Bayesian analysis. The experimental data (black line) are fitted with theoretical dynamic structure factor calculations (blue line).

DETAILS OF THE MCMC PROCEDURE

To account for the inverse problem instability, a robust method for exploring the complex multi-parameter space is to utilize Bayesian inference using Markov-Chain Monte Carlo (MCMC) [6, 7]. Given a specific set of parameters, $\Theta(T_e, \rho, Z_H, Z_C, r_c)$, the MCMC process calculates the likelihood of these producing the given experimental spectrum, I_{exp} , as,

$$P(\Theta|I_{\text{exp}}) = \frac{P(I_{\text{exp}}|\Theta)P(\Theta)}{P(I_{\text{exp}})}, \quad (2)$$

where $P(\Theta)$ is the prior distribution of possible parameters and $P(I_{\text{exp}})$ is the marginal likelihood of the observed data over all possible parameters. The forward model likelihood, $P(I_{\text{exp}}|\Theta) = e^{-\beta_{\text{cost}}}$, gives an acceptance percentage for each Θ , allowing convergence to be found on a parameter space that falls within the experimental noise.

Separate MCMC explorations were run for the XRTS and XRD data, respectively. Each assumed two uniform plasma conditions, one representing the WDM conditions and the other the blow-off conditions. The blow-off conditions were assumed to be fixed at $T_e = 36$ eV, $Z_C = 4$, $Z_H = 1$ and $\rho = 0.01$ g/cm³. The regions were weighted by the parameter r_c , which is equal to the fraction of scattering from WDM determined to be contributing to the overall signal. The plasma parameter prior, $P(\Theta)$, assumed a uniform distribution with linear sampling for the hydrogen ionization, $0 \leq Z_H \leq 1$, carbon ionization $0 \leq Z_C \leq 6$, and density $0.5 \leq \rho$ (g/cm³) ≤ 3 , whilst a logarithmic sampling was taken for the temperature $0.05 \leq T_e = T_i$ (eV) ≤ 7 . The range of accepted fits is shown as blue-shaded regions in figures XRTS and XRD figures in the main manuscript.

To perform the MCMC analysis, appropriate cost calculations, β_{cost} , must be selected to allow for parameter convergence that is representative of the data. For the XRTS MCMC analysis, the cost function used to determine the appropriateness of each MCMC spectra was a weighted soft boundary,

$$\beta_{\text{XRTS}} = \exp \left(-\max \frac{I_{\text{exp}} - I_{\text{fit}}}{\sqrt{2}\sigma I_{\text{exp}}} \right)^2 \quad (3)$$

where I_{exp} is the experimental signal, I_{fit} is the MCMC fit, and σ is selected to allow the range of accepted fits to be representative of the noise on the data. For the XRTS fitting, a σ of 0.02 was chosen where the signal is greater than 10% of the peak value, and 0.08 otherwise. For the XRD analysis the cost function the cost function, β_{XRD} , was not weighted (i.e. the I_{exp} was removed from the denominator in equation 3). This is done as the XRD data does not contain a significant difference in the signal level across the spectrum, as is the case with XRTS. The σ taken for this XRD MCMC exploration was 0.012.

Figure 2 shows the resultant converged probability density functions of the plasma parameters for both the XRTS and XRD analysis. The probability density functions, $\Pr(\rho, T_e, Z_C, Z_H)$, for each diagnostic, can be combined to find a mutually agreed parameter space. This joint probability is defined as,

$$\Pr_j(\rho, T_e, Z_C, Z_H) = \frac{\Pr_x(\rho, T_e, Z_C, Z_H) \times \Pr_d(\rho, T_e, Z_C, Z_H)}{\sum_{\rho, T_e, Z_C, Z_H} [\Pr_x(\rho, T_e, Z_C, Z_H) \times \Pr_d(\rho, T_e, Z_C, Z_H)]}, \quad (4)$$

where x and d denote the XRTS and XRD MCMC analysis, respectively. This combined parameter distribution can be collapsed into 2-D and 1-D space and is shown in red in Figure 2. The 1σ errors of each parameter's joint probability density function, i.e., $\Pr_j(\rho)$, are given in Table I in the main manuscript.

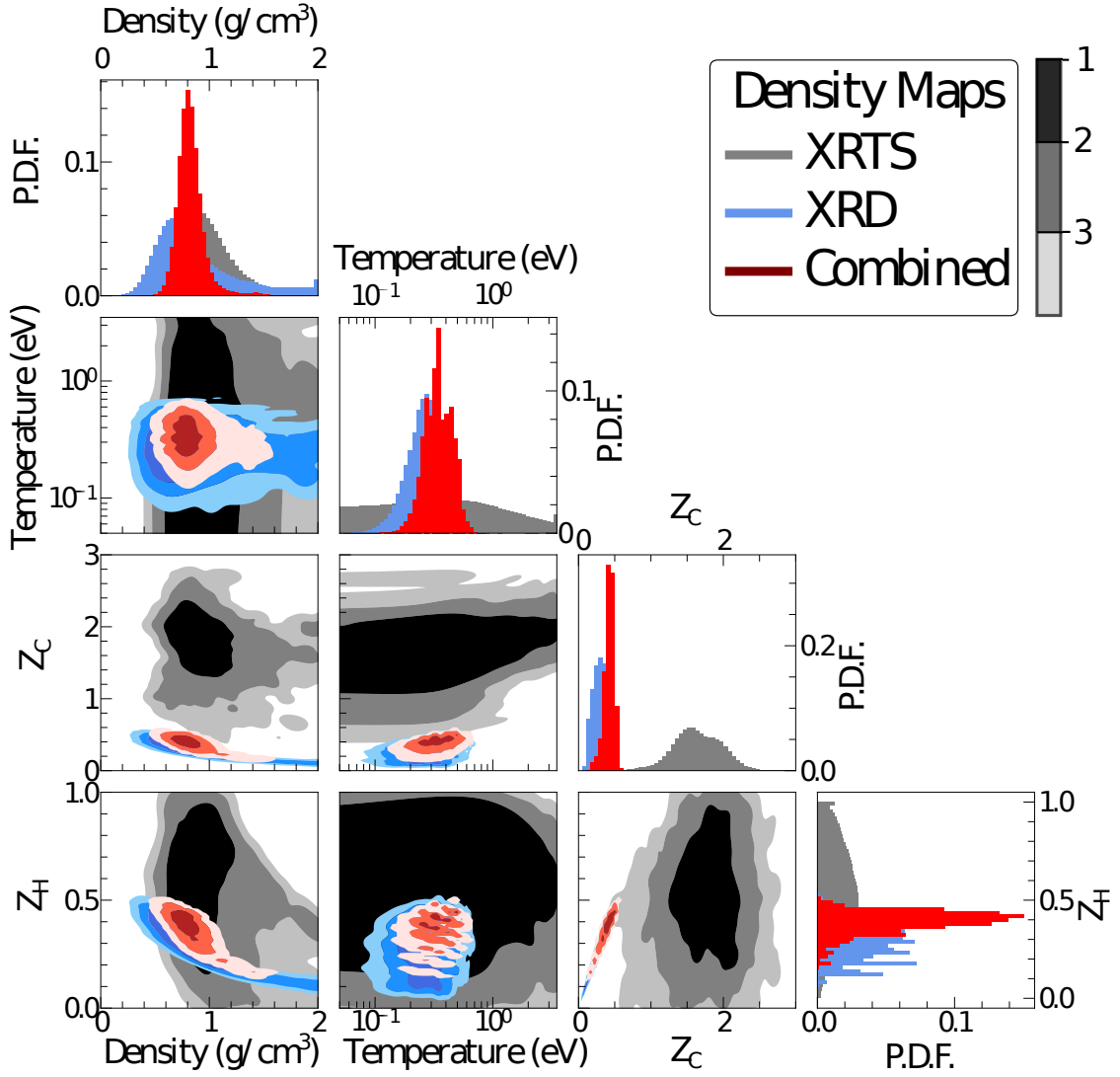


FIG. 2. Variation in the converged temperature, density, and ionizations of the WDM region extracted from the MCMC analysis of the XRTS (in gray) and XRD (in blue) data. The lower quadrant shows the 2-D probability distribution functions for each diagnostic. Their corresponding joint distributions, as defined by equation 4, are superimposed as red heat maps. The diagonal plots show the 1-D probability distribution histograms for each parameter.

IDENTIFICATION OF BLOW-OFF PLASMA CONDITIONS

In order to extract the thermodynamic conditions of the warm dense matter target, the conditions of the surrounding blow-off plasma were identified. The temperature of the blow-off plasma is well constrained by the slope of the high-energy wing of the Compton feature (see Fig. 3a). From this slope, we identify the temperature of the blow-off plasma to be 36 ± 5 eV. Secondly, we note that it is not necessary to precisely define the density of the blow-off plasma, as the shape of the spectrum is insensitive to density variations at densities less than 0.05 g/cm^3 , as demonstrated in Fig. 3b. Finally, we estimate the ionization of the carbon and hydrogen using PROPACEOS tables [8], which suggest ionizations of $Z_H = 1$ and $Z_C = 4$.

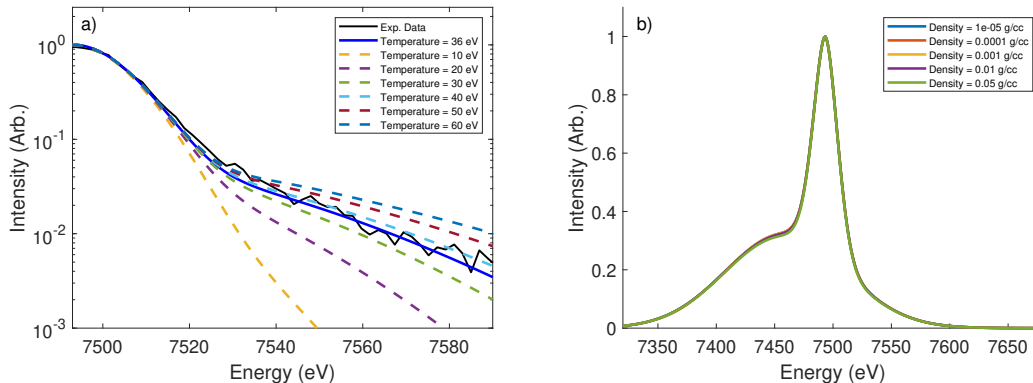


FIG. 3. Sensitivity of XRTS spectrum for the blow-off plasma to variation in (a) temperature and (b) density.

ENERGY DISPERSION OF THE HIGH-RESOLUTION SPECTROMETER

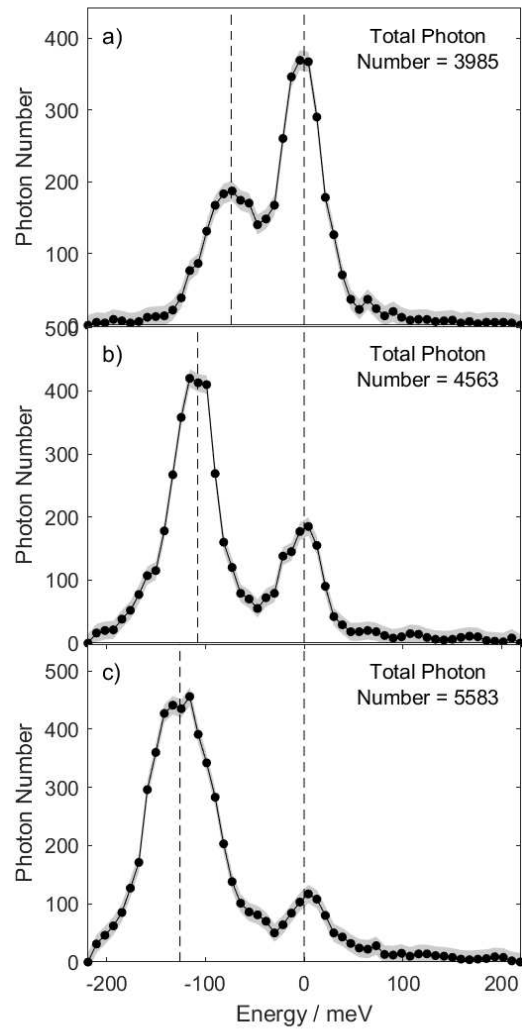


FIG. 4. The high-resolution spectrometer was calibrated by measuring the acoustic phonon frequencies in polycrystalline diamond, leading to a dispersion of 8.2 meV/pixel. Additional details are given in McBride *et al.* [9]

ENERGY DISPERSION OF THE X-RAY THOMSON SCATTERING SPECTROMETER

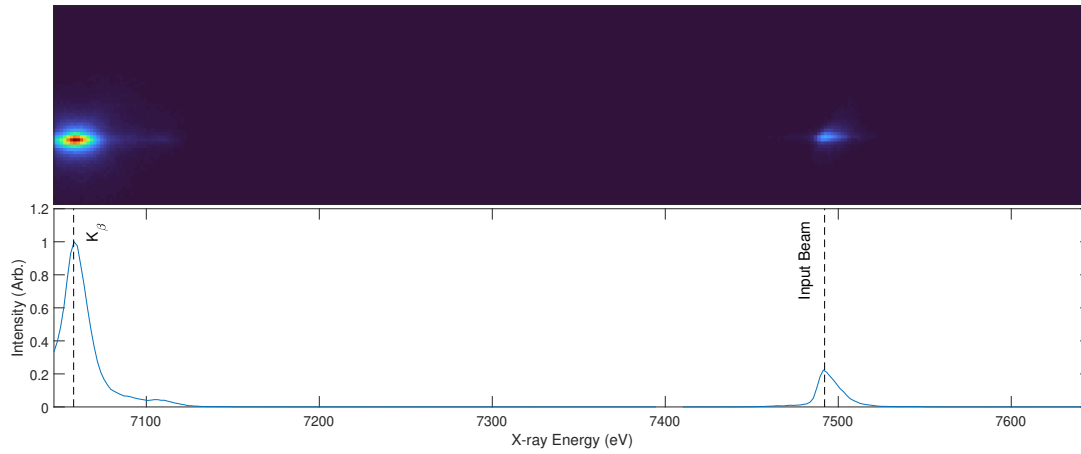


FIG. 5. The dispersion of the X-ray Thomson Scattering (XRTS) diagnostic was found to be 1.93 ± 0.04 eV/px, calibrated using fluorescence of the $K_{\beta 1}$ line of iron located at 7057.98 eV together with the input energy of the X-ray beam at 7492 ± 10 eV, where the uncertainty in the input energy measurement accounts for the finite width of the SASE bandwidth.

X-RAY DIFFRACTION (XRD) CALIBRATION AND ANALYSIS

The powder patterns were processed and integrated using the Dioptas software [10]. The relationship between pixel position and scattering angle was calibrated using polycrystalline LaB6, as shown in figure 6. A dark field, taken on shots without X-ray irradiation, was subtracted from each image. The data was further processed to correct for the solid angle of each pixel facing the scattering target, transmission through a filter consisting of 50 μm of Al and 125 μm polyimide, and a polarization factor $(1 - \sin^2(\theta) \cos^2(\phi))$, where θ is the scattering angle and ϕ is the angle between the plane of the scattering vectors and the polarization of the incoming X-rays. In addition, the non-linear response of a few hot pixels was identified and removed by running a high-pass filter over the data to identify high-frequency noise common to multiple images taken at multiple time delays. In figure 7, we confirm that this procedure leaves the shape of the spectrum unchanged.

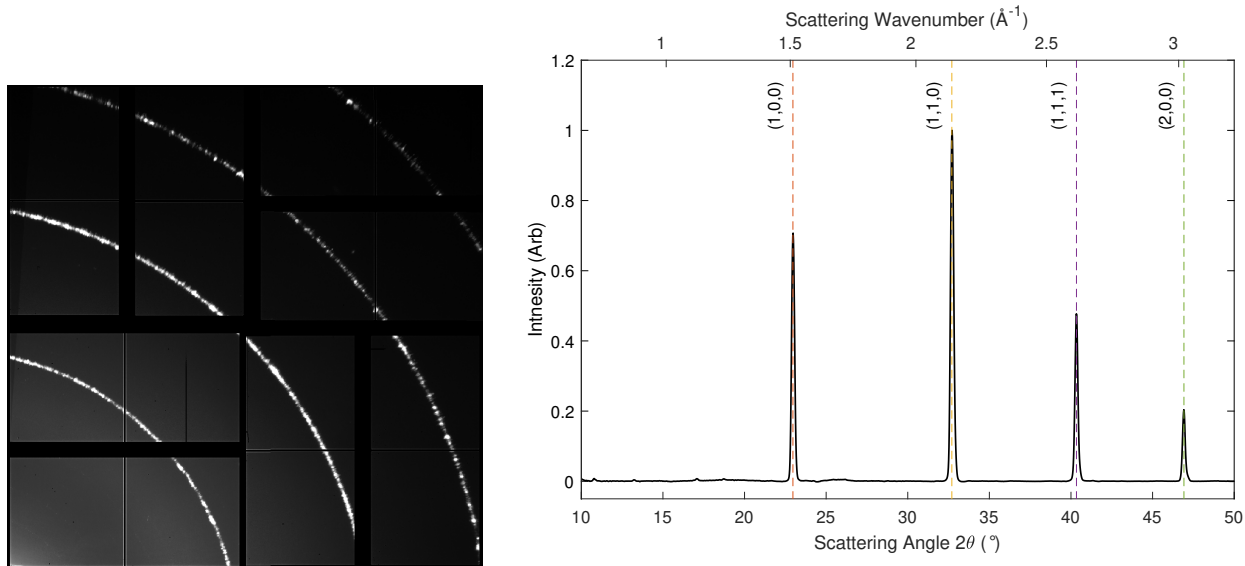


FIG. 6. The large area detector was calibrated using X-ray diffraction from polycrystalline LaB6. (Left) Raw data showing the Debye-Scherrer rings from LaB6 at an X-ray energy of 7492.1 eV. (Right) Transformation of the 2-D diffraction pattern onto the scattering angle together with the predicted position of the first four diffraction lines in LaB6.

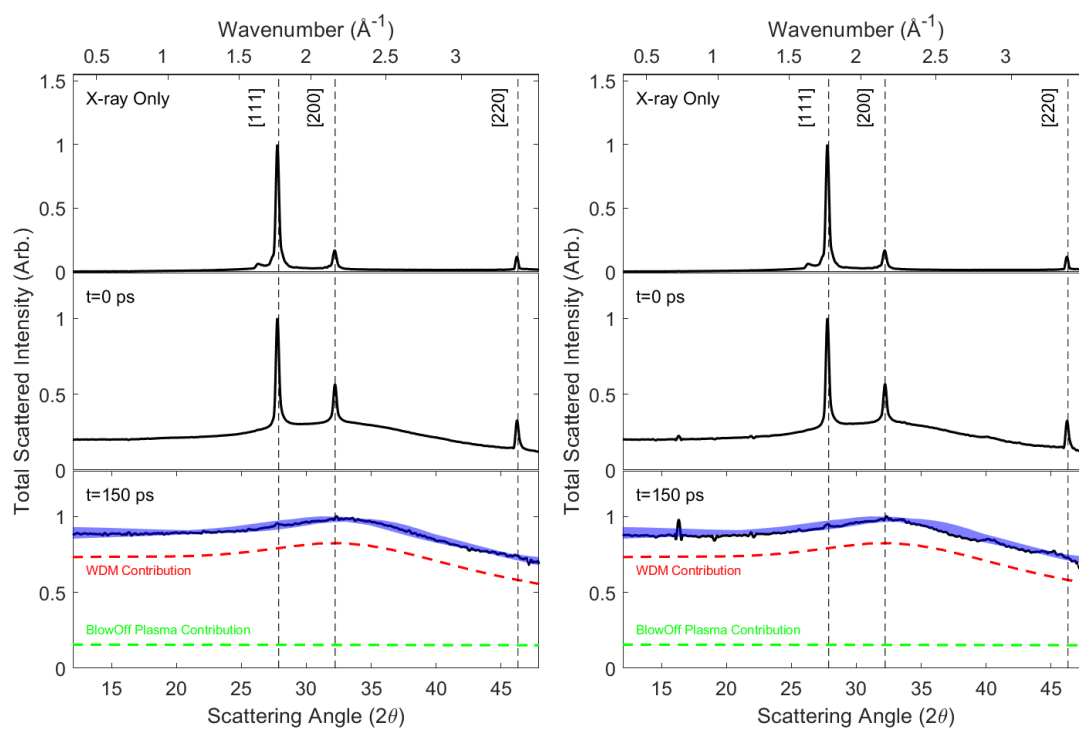


FIG. 7. The XRD data shown in the main manuscript is reproduced (left) with and (right) without the subtraction of hot pixels. Importantly, this process leaves the shape of the spectrum, including the Bragg peak location and heights, unchanged.

FITTING THE SCATTERING SPECTRA

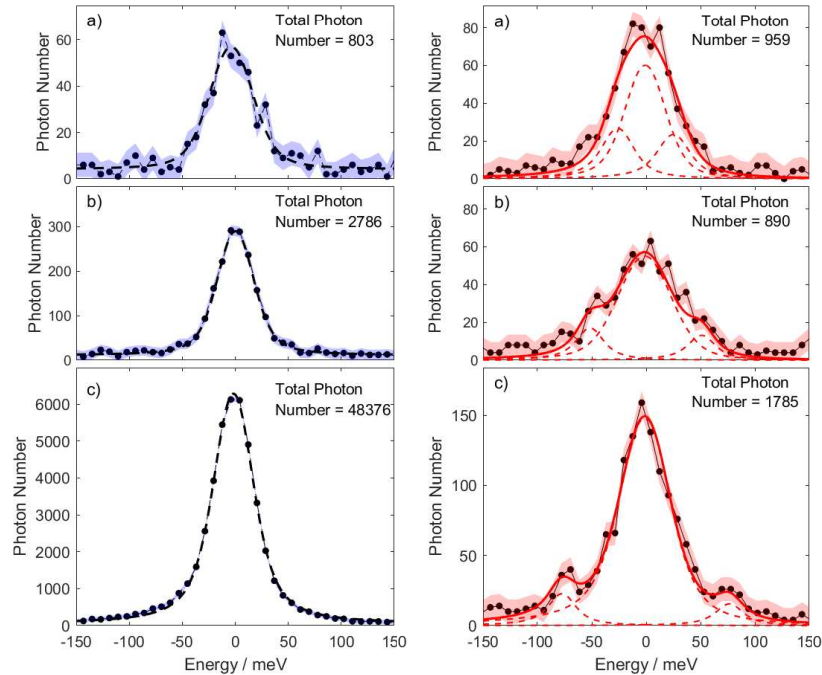


FIG. 8. (Left) High-resolution energy-resolved scattering data at (a) 10° , (b) 20° , and (c) 30° for undriven methane. The spectra were collected at 120 Hz over 217028 events, with the total number of detected photons given. In each case, the instrument function is fitted to a pseudo-Voigt profile, with a width of (a) 49 meV, (b) 42 meV, and (c) 46 meV. These numbers are close to the nominal value of 46 meV. (Right) Experimental results from driven methane taken from the main manuscript. The data consists of 5965 events, and the number of photons collected in each case is shown. The spectra were well-fitted by combining three Voigt profiles, as shown. The Brillouin peaks are located at (d) 26 meV, (e) 51 meV, and (f) 77 meV, consistent with an acoustic wave speed of 5.9 km/s.

-
- [1] G. Gregori, S. H. Glenzer, W. Rozmus, R. W. Lee, and O. L. Landen, Theoretical model of x-ray scattering as a dense matter probe, *Phys. Rev. E* **67**, 026412 (2003).
 - [2] D. Pines and D. Bohm, A collective description of electron interactions: II. Collective vs individual particle aspects of the interactions, *Phys. Rev.* **85**, 338 (1952).
 - [3] S. H. Glenzer and R. Redmer, X-ray Thomson scattering in high energy density plasmas, *Rev. Mod. Phys.* **81**, 1625 (2009).
 - [4] G. Gregori, S. H. Glenzer, F. J. Rogers, S. M. Pollaine, O. L. Landen, C. Blancard, G. Faussurier, P. Renaudin, S. Kuhlbrodt, and R. Redmer, Electronic structure measurements of dense plasmas, *Physics of Plasmas* **11**, 2754 (2004), <https://doi.org/10.1063/1.1689664>.
 - [5] G. Gregori, A. Ravasio, A. Höll, S. Glenzer, and S. Rose, Derivation of the static structure factor in strongly coupled non-equilibrium plasmas for X-ray scattering studies, *High Energy Density Physics* **3**, 99 (2007).
 - [6] M. F. Kasim, T. P. Galligan, J. Topp-Mugglestone, G. Gregori, and S. M. Vinko, Inverse problem instabilities in large-scale modeling of matter in extreme conditions, *Physics of Plasmas* **26**, 112706 (2019), <https://doi.org/10.1063/1.5125979>.
 - [7] H. Poole, D. Cao, R. Epstein, I. Golovkin, T. Walton, S. X. Hu, M. Kasim, S. M. Vinko, J. R. Rygg, V. N. Goncharov, G. Gregori, and S. P. Regan, A case study of using x-ray Thomson scattering to diagnose the in-flight plasma conditions of DT cryogenic implosions, *Physics of Plasmas* **29**, 072703 (2022), <https://doi.org/10.1063/5.0072790>.
 - [8] J. MacFarlane, I. Golovkin, and P. Woodruff, HELIOS-CR – A 1-D radiation-magnetohydrodynamics code with inline atomic kinetics modeling, *Journal of Quantitative Spectroscopy and Radiative Transfer* **99**, 381 (2006).
 - [9] E. E. McBride, T. G. White, A. Descamps, L. B. Fletcher, K. Appel, F. P. Condamine, C. B. Curry, F. Dallari, S. Funk, E. Galtier, M. Gauthier, S. Goede, J. B. Kim, H. J. Lee, B. K. Ofori-Okai, M. Oliver, A. Rigby, C. Schoenwaelder, P. Sun, Th. Tschentscher, B. B. L. Witte, U. Zastra, G. Gregori, B. Nagler, J. Hastings, S. H. Glenzer, and G. Monaco, Setup for meV-resolution inelastic X-ray scattering measurements and X-ray diffraction at the Matter in

Extreme Conditions endstation at the Linac Coherent Light Source, *Review of Scientific Instruments* **89**, 10F104 (2018), <https://doi.org/10.1063/1.5039329>.

- [10] C. Prescher and V. B. Prakapenka, DIOPRAS: A program for reduction of two-dimensional X-ray diffraction data and data exploration, *High Pressure Research* **35**, 223 (2015), <https://doi.org/10.1080/08957959.2015.1059835>.